Atmos. Meas. Tech. Discuss., 6, 9819–9855, 2013
www.atmos-meas-tech-discuss.net/6/9819/2013/
doi:10.5194/amtd-6-9819-2013

Atmospheric Measurement Techniques Discussions

An improved algorithm for cloud base detection by ceilometer over the ice sheets

K. Van Tricht[1], I. V. Gorodetskaya[1], S. Lhermitte[1,2], D. D. Turner[3], J. H. Schween[4], and N. P. M. Van Lipzig[1]

[1]Department of Earth and Environmental Sciences, KU Leuven, Heverlee, Belgium
[2]Royal Netherlands Meteorological Institute (KNMI), Regional Climate, De Bilt, the Netherlands
[3]NOAA National Severe Storms Laboratory, USA
[4]Meteorological Institute, Köln University, Cologne, Germany

Received: 8 October 2013 – Accepted: 30 October 2013 – Published: 14 November 2013

Correspondence to: K. Van Tricht (kristof.vantricht@ees.kuleuven.be)

Published by Copernicus Publications on behalf of the European Geosciences Union.

Abstract

Optically thin ice clouds play an important role in polar regions due to their effect on cloud radiative impact and precipitation on the surface. Cloud bases can be detected by lidar-based ceilometers that run continuously and therefore have the potential to provide basic cloud statistics including cloud frequency, base height and vertical structure. Despite their importance, thin clouds are however not well detected by the standard cloud base detection algorithm of most ceilometers operational at Arctic and Antarctic stations. This paper presents the Polar Threshold (PT) algorithm that was developed to detect optically thin hydrometeor layers (optical depth $\tau \geq 0.01$). The PT algorithm detects the first hydrometeor layer in a vertical attenuated backscatter profile exceeding a predefined threshold in combination with noise reduction and averaging procedures. The optimal backscatter threshold of $3 \times 10^{-4}\,\mathrm{km}^{-1}\,\mathrm{sr}^{-1}$ for cloud base detection was objectively derived based on a sensitivity analysis using data from Princess Elisabeth, Antarctica and Summit, Greenland. The algorithm defines cloudy conditions as any atmospheric profile containing a hydrometeor layer at least 50 m thick. A comparison with relative humidity measurements from radiosondes at Summit illustrates the algorithm's ability to significantly differentiate between clear sky and cloudy conditions. Analysis of the cloud statistics derived from the PT algorithm indicates a year-round monthly mean cloud cover fraction of 72 % at Summit without a seasonal cycle. The occurrence of optically thick layers, indicating the presence of supercooled liquid, shows a seasonal cycle at Summit with a monthly mean summer peak of 40 %. The monthly mean cloud occurrence frequency in summer at Princess Elisabeth is 47 %, which reduces to 14 % for supercooled liquid cloud layers. Our analyses furthermore illustrate the importance of optically thin hydrometeor layers located near the surface for both sites, with 87 % of all detections below 500 m for Summit and 80 % below 2 km for Princess Elisabeth. These results have implications for using satellite-based remotely sensed cloud observations, like CloudSat, that may be insensitive for hydrometeors near the surface. The results of this study highlight

AMTD
6, 9819–9855, 2013

the potential of the PT algorithm to extract information in polar regions about a wide range of hydrometeor types from measurements by the robust and relatively low-cost ceilometer instrument.

1 Introduction

Clouds have an important effect on the polar climates. Locally, polar tropospheric clouds influence the energy and mass balance of the ice sheets (Bintanja and Van den Broeke, 1996; Intrieri, 2002; Bromwich et al., 2012; Kay and L'Ecuyer, 2013). However, changes in cloud properties may modify the climate of regions well beyond these high latitudes as well (Lubin et al., 1998). Climate models still have difficulties in correctly projecting the polar climate, an important part of which is due to uncertainties in their cloud parameterizations such as macro- and microphysical properties (Bennartz et al., 2013; Ettema et al., 2010; Gorodetskaya et al., 2008) and feedback mechanisms (Dufresne and Bony, 2008).

Despite the great importance of clouds on the surface mass and energy balance, cloud research at these high latitudes is still hampered by a lack of sufficient cloud observations. The harsh and remote environment in Arctic and Antarctic regions has limited the amount of ground stations used for climatic research. The research sites that are present are equipped with robust instruments that can withstand very cold conditions. One of the most robust instruments that is used for observing clouds is the ceilometer, a ground-based low-power laser device. It can operate continuously in all weather conditions (Hogan et al., 2003) and is one of the more abundant (> 10) instruments at Arctic and Antarctic stations, including at Summit, Atqasuk, Barrow, Ny-Ålesund (Arctic study sites) and at Princess Elisabeth, Rothera, Halley (Antarctic study sites) (Bromwich et al., 2012; Shanklin et al., 2009; Shupe et al., 2011).

A macrophysical property inferred from ceilometer data is the cloud base height (CBH) which is defined as the lower boundary of a cloud. The CBH is used for different purposes, including visibility determination, the study of cloud statistics (e.g. cloud

AMTD
6, 9819–9855, 2013

heights) and validation of other remotely sensed cloud measurements, such as satellite observations. Most often, the CBH is calculated by built-in algorithms developed by the instrument's manufacturers such as the Vaisala cloud base detection algorithm (Garrett and Zhao, 2013; Shupe et al., 2011). However, these built-in algorithms are primarily designed to report the altitude where the horizontal visibility to a pilot is drastically reduced (Flynn, 2004). These algorithms therefore struggle to identify cloud bases over the ice sheets, where clouds are often optically thin. Bernhard (2004) showed that at the South Pole 71 % of all clouds have an optical depth between 0 and 1 and the Arctic clouds are also frequently optically thin (Sedlar et al., 2010; Shupe and Intrieri, 2004). Despite the low optical depth of ice clouds, their detection is important in terms of determination of the cloud radiative impact or potential precipitation growth (Sun and Shine, 1995; Curry et al., 1996; Pruppacher and Klett, 2010; Kay and L'Ecuyer, 2013).

Ceilometers typically detect cloud bases at a distinct height and increasing backscatter (see e.g. Fig. 1). Although there are clearly regions with increased backscatter below, the standard Vaisala CBH detection algorithm reports the CBH at rather higher levels, that are likely related to liquid-containing portions in case of a mixed-phase cloud (Bromwich et al., 2012; Curry et al., 2000; Hobbs and Rangno, 1998; Pinto, 1998; Uttal et al., 2002; Verlinde et al., 2007). The optically much thicker top layer most probably related to supercooled liquid has a much higher backscatter coefficient compared to the optically thin layer below, leading to incorrectly reported CBH by the conventional algorithms. Other CBH detection algorithms have been developed that use different approaches to infer CBH compared to the standard algorithms. An example is the temporal height tracking (THT) algorithm developed by Martucci et al. (2010), that uses backscatter maxima and backscatter gradient maxima to calculate the CBH. However, this algorithm has not been designed to detect optically thin clouds in a polar atmosphere, which is apparent from the CBH detections by the THT algorithm in Fig. 1. Other more advanced instruments are also reporting CBH, such as the Micropulse Lidar (MPL) (e.g., Clothiaux et al., 1998; Campbell et al., 2002), but these instruments are less abundant over the different study sites in the Arctic

AMTD
6, 9819–9855, 2013

and Antarctic, mostly due to their complexity and higher cost (Barnes et al., 2003). An algorithm that is capable of calculating the CBH from ceilometer data in polar regions, including the detection of optically very thin hydrometeor features, therefore would greatly improve cloud statistics in these areas.

The goal of this study is to develop a simple method that uses ceilometer measurements and that is sensitive enough to detect these optically thin ice clouds abundant in polar regions. We propose to use a fairly straightforward backscatter threshold approach. We describe here the theoretical framework of the new algorithm, the determination of the optimal backscatter threshold and results that were obtained by applying the algorithm on the ceilometer measurements at an Arctic and an Antarctic station.

2 Data

2.1 Study area

The locations of the two research stations used in this study are shown in Fig. 2. They were chosen based on their characteristic climatology and available instrumentation.

The Antarctic data originate from the Princess Elisabeth (PE) station, located in the escarpment zone of Dronning Maud Land, East-Antarctica (Pattyn et al., 2009). The station is situated on the Utsteinen Ridge near the Sør Rondane mountains at an elevation of 1382 m a.s.l., 220 km inland (71.95° S, 23.35° E). Its location makes the station well protected from katabatic winds, however with a significant influence of coastal storms 50 % of the time (Gorodetskaya et al., 2013a). Cloud measurements are carried out in the context of the HYDRANT project, for which a unique instrument set has been installed, including a ceilometer, an uplooking infrared radiation pyrometer, a vertically pointing micro rain radar and an automatic weather station (Gorodetskaya et al., 2013b). Data are currently limited to summertime

AMTD
6, 9819–9855, 2013

cases due to power outages in wintertime. Cases used in this study are selected from December to March between 2010 and 2013.

The Arctic cloud data were recorded at the Summit station atop the Greenland ice sheet, 3250 m a.s.l. (72.6° N, 38.5° W). The station is located 400 km inland from the nearest coastline, making it a continental study site. The atmosphere on top of the ice sheet is extremely dry and cold, while many cloud properties are comparable to other Arctic regions (Shupe et al., 2013). The station is equipped with an extensive instrument set, including both passive as well as active sensors and a twice-daily radiosonde program, making this research site unique for cloud observing purposes. The cases used in this study are year-round measurements between 2010 and 2012 as part of the Integrated Characterization of Energy, Clouds, Atmospheric state, and Precipitation at Summit (ICECAPS) project (Shupe et al., 2013).

2.2 Ceilometer

The Greenland Summit station is equipped with a Vaisala CT25K laser ceilometer, while the Antarctic PE station has the newer Vaisala CL31 laser ceilometer. These ceilometers both are devices emitting low-power laser pulses. Their vertical range extends up to 7.5 km for both. The CL31 instrument is more sensitive than the CT25K because it has a higher average emitted power (12 mW vs. 8.9 mW). Further technical details of both ceilometers are given in Table 1.

The output used in this study is the range and sensitivity corrected attenuated backscatter coefficient β_{att} ($\text{km}^{-1}\,\text{sr}^{-1}$), which describes how much light from the emitted laser pulse is scattered into the backward direction, not corrected for attenuation by extinction. It is the product of the volume backscatter coefficient β at a certain height range and the squared transmittance of the atmosphere between the ceilometer and the scattering volume (Münkel et al., 2006). It is found after multiplying the received power by all instrument specific factors, constants and the squared distance. Since the transmittance of the atmosphere is in general unknown, conversion of attenuated backscatter β_{att} to corrected backscatter β is not straightforward. The

AMTD
6, 9819–9855, 2013

returned signal of the pulses is averaged over a period of 15 s which determines the temporal resolution of the measurements. The vertical resolution is 30 m for the CT25K at Summit and 10 m for the CL31 at PE.

An additional difference between both ceilometers is the precision of the reported backscatter. The CT25K reports integer values of attenuated backscatter in $1 \times 10^{-4}\,km^{-1}\,sr^{-1}$, while the CL31 reports in $1 \times 10^{-5}\,km^{-1}\,sr^{-1}$, i.e. a factor 10 more precise. Calibration of the raw CT25K data was necessary, which was done based on the autocalibration method by O'Connor et al. (2004). They showed that supercooled water layers have essentially the same characteristics as warm stratocumulus clouds for which the method was developed. We therefore selected cases with supercooled water layers that completely attenuate the laser beam, for which the lidar ratio is assumed to be constant and known (see Sect. 4.3). We filtered these cases to retain profiles with a minimum amount of ice precipitation, since ice precipitation violates the constant lidar ratio assumption. Due to the low beam divergence of the CT25K ceilometer (Table 1), the effect of multiple scattering is small. Applying the autocalibration method resulted in a scale factor of 3. The inevitable presence of ice in certain profiles invalidates some of the assumptions in the O'Connor method and introduces an additional uncertainty in the calibrated data. Despite this, the autocalibration method significantly improved the large biases that were encountered in the raw CT25K measurements. After calibration of the Summit ceilometer, the minimum detection limit is $3 \times 10^{-4}\,km^{-1}\,sr^{-1}$, while $1 \times 10^{-5}\,km^{-1}\,sr^{-1}$ is the minimum detection limit for the PE ceilometer.

2.3 Radiosondes

Among the observations at Summit is a twice-daily radiosonde program for characterizing the atmospheric state (Shupe et al., 2013). Relative humidity (RH) is measured with the Vaisala RS92-K and RS92-SGP sondes and reported at a temporal resolution of 2 s, resulting in a vertical RH profile. Due to the low atmospheric

AMTD
6, 9819–9855, 2013

temperatures, we report the RH with respect to ice (RH_{ice}), using Tetens formulation as described by Murray (1967).

The high uncertainty of the RH measurements at cold temperatures (dry bias) for the RS80 and RS90 sondes (Miloshevich et al., 2001; Rowe et al., 2008), is mostly resolved with the RS92 sondes (Suortti et al., 2008). Yet, solar radiation heating of the sensors may occur due to the absence of a silver cap found on the RS80s that acts as a radiation shield, leading to a dry bias (Wang et al., 2013). Vömel et al. (2007) who first quantified this bias however indicated that this issue is less severe in polar regions because the solar elevation angle is lower at high latitudes. Suortti et al. (2008) moreover identified the RS92 sonde as being superior to other radiosonde sensors.

3 Methodology

The development of a CBH detection algorithm depends on which atmospheric features are considered to be a cloud. In this study a cloud is defined to be any hydrometeor layer at least 50 m thick in the atmospheric column detected by the ceilometer. This includes ice particles and supercooled liquid droplets as well as any form of precipitation, all of which are important for the radiative budget and mass balance of the ice sheets (Bintanja and Van den Broeke, 1996; Bromwich et al., 2012; Curry et al., 1996; Intrieri, 2002; Pruppacher and Klett, 2010; Sun and Shine, 1995). The CBH detection algorithm then determines the height of the first detectable occurrence of hydrometeors in a layer at least 50 m thick.

Our goal was to develop a cloud detection method that is able to detect the CBH in optically thin layers even when liquid is present higher in the profile. The new Polar Threshold (PT) algorithm therefore compares the measured attenuated backscatter to a predefined backscatter threshold. This allows the algorithm to be sensitive to optically thin hydrometeor layers characterized by low attenuated backscatter returns and a lack of sharp gradients. This approach differs from the standard Vaisala algorithm (Flynn, 2004) and the THT algorithm (Martucci et al., 2010) that look at visibility or backscatter

AMTD
6, 9819–9855, 2013

(gradient) maxima. A threshold method has been used before, e.g. by Platt et al. (1994). However, they used a multiple of the standard deviation of the background fluctuations as a threshold to be exceeded by the attenuated backscatter signal, but as the variability in the background signal of clear polar air is small, we propose an absolute attenuated backscatter threshold to be exceeded for CBH detection. In this section we first describe the noise reducing and averaging procedures to be carried out prior to the actual CBH detection, followed by the principle of the PT algorithm and the procedure to determine the optimal backscatter threshold.

3.1 Noise reduction and averaging

For a sensitive algorithm to work properly noise levels should be reduced and useful signal should be emphasized. The ceilometer being a low-power laser instrument inherently reports attenuated backscatter with a considerate degree of noise (e.g., Clothiaux et al., 1998). Especially the decrease of signal with range, further exacerbated by the range correction (evident from the lidar equation in e.g. Münkel et al., 2006) leads to increasing noise levels higher in the profile. We therefore first remove noisy data detected by investigating the signal-to-noise ratio (SNR) and afterwards average the raw ceilometer attenuated backscatter data. The SNR was calculated for every separate height range bin as:

$$\mathrm{SNR} = \frac{\mathrm{mean}(\beta_{\mathrm{att}})_{10\,\mathrm{min}}}{\mathrm{std}(\beta_{\mathrm{att}})_{10\,\mathrm{min}}}, \quad (1)$$

which is the ratio of the mean of an attenuated backscatter interval of 10 min at a certain height in the profile over the standard deviation (std) of that backscatter interval. The atmospheric fluctuations in this interval are small compared to the instrument noise such that the standard deviation over the interval mainly contains internal noise from the instrument. This method is different from the common technique for lidars to estimate the instrument's noise level from the background light (see e.g. Heese et al., 2010), but as Vaisala ceilometers report background light only as voltage, this method

AMTD
6, 9819–9855, 2013

is not applicable. Noisy data are characterized by a low mean backscatter (averaged over positive and negative values) and a high standard deviation, resulting in low SNR values. The SNR threshold was set to 1 as was also done by Heese et al. (2010), and pixels with a lower SNR were removed. In a second step, the noise-reduced data were smoothed by applying a running mean over an interval of 2.5 min. Due to the impact of the averaging method on the results as reported in Stachlewska et al. (2012), we varied the running mean interval between 1 and 15 min, but the impact on our results was below 1 %. Fig. 3 shows an example ceilometer attenuated backscatter image with a typical backscatter profile before and after the noise reduction and averaging procedures.

3.2 Polar threshold algorithm

The PT algorithm processes every vertical profile separately and compares the attenuated backscatter of each range bin to a backscatter threshold in a bottom-up approach. The first 60 m (2 range bins at Summit, 6 range bins at PE) however are excluded to minimize the effects of shallow blowing snow layers. The CBH detection is triggered if the attenuated backscatter at a certain height in the vertical profile exceeds the threshold. After the trigger, the algorithm also considers the mean attenuated backscatter 50 m above the trigger point (60 m for the Summit ceilometer). If the backscatter value at this elevated height also exceeds the threshold, the height of the trigger point is set as the CBH. This ensures a certain amount of robustness of the signal at the detected CBH, meaning that a hydrometeor layer should have a minimum geometrical thickness to be detectable by the algorithm. If not, the algorithm proceeds with the next range bin in the profile. If the end of the vertical profile is reached without a valid CBH detection, the profile is marked as clear sky. This approach was found to perform best in identifying the base of optically thin hydrometeor layers compared to other algorithms. Figure 4 shows the ideal result of the PT-derived CBH compared to the Vaisala and THT algorithms for an example attenuated backscatter profile. The original (not noise-reduced) ceilometer data are shown. It is evident that

AMTD
6, 9819–9855, 2013

the threshold-based PT algorithm can be triggered at much lower backscatter values occurring at the base of an optically thin ice layer compared to the other algorithms that are triggered much higher in the profile, most probably at a liquid-containing layer. In the next section, the optimal threshold to be used by the PT algorithm in order to achieve results as in Fig. 4, is objectively determined.

3.3 Determining optimal threshold

The CBH detection by the PT algorithm strongly depends on the backscatter threshold that is used. The optimal threshold is one that allows the detection of hydrometeor layers with a low optical depth while not triggering the algorithm in clear sky conditions. To make an objective threshold choice, we performed a sensitivity analysis by varying the backscatter threshold between the detection limits of the ceilometers and the maximum backscatter value in the data and evaluating the effect on the cloud detections. The total number of profiles containing a cloud that is detected by the PT algorithm over all cases (= the total number of detections) was calculated for each threshold.

The results of the sensitivity analysis for PE are shown in Fig. 5a. At a backscatter threshold just below $3 \times 10^{-4}\,\mathrm{km}^{-1}\,\mathrm{sr}^{-1}$ there is a sharp decrease in total number of detections. At this transition, the total number of detections is approximately halved, which is related to the fact that PE experiences synoptic influence favouring cloud occurrence about 50 % of the time (Gorodetskaya et al., 2013a). The backscatter threshold at $3 \times 10^{-4}\,\mathrm{km}^{-1}\,\mathrm{sr}^{-1}$ effectively represents the minimum concentration of hydrometeors detectable by the ceilometer distinguishing cloudy from clear sky profiles. The lowest detection limit after calibration of the ceilometer at Summit corresponds to the backscatter threshold determined for the PE ceilometer (Fig. 5b). Therefore, we used identical backscatter thresholds for PE and Summit.

The amount of backscatter that reaches the detector is a function of the extinction profile and thus of the optical depth of the atmosphere (Roy et al., 1993). Further increasing the threshold therefore increases the optical depth of the detected clouds

AMTD
6, 9819–9855, 2013

and influences both the amount and height of the detected cloudy profiles. Even if the amount of detections does not significantly vary with a changing threshold (flat parts of the curves in Fig. 5), a higher threshold triggers the CBH detection higher in the backscatter profiles, leading to overall higher CBH results. For example, increasing the threshold from $3 \times 10^{-4}\,km^{-1}\,sr^{-1}$ to $30 \times 10^{-4}\,km^{-1}\,sr^{-1}$ at Summit decreases the amount of detections by 10 % and increases the mean CBH by 70 m, while at PE the amount of detections is decreased by only 2 %, though the mean CBH increases by 190 m. As our purpose is to detect the optically thinnest detectable hydrometeors lowest in the profile, we choose the lowest backscatter threshold indicating the presence of hydrometeors ($3 \times 10^{-4}\,km^{-1}\,sr^{-1}$ for both the PE and Summit ceilometers).

4 Results

4.1 Applying the PT algorithm

The PT algorithm was applied to all available cases at the study sites. Example CBH results for the three tested algorithms are shown in Fig. 6 with the 8 March 2010 case for PE and the 19 December 2010 case for Summit. These cases were chosen because they represent different atmospheric conditions on which the PT algorithm could be tested. These conditions include clear sky profiles, ice layers and polar mixed-phase cloud structures (optically thicker layer most probably due to the presence of supercooled liquid over an optically thinner but geometrically thicker ice-only layer). The Summit ceilometer data in Fig. 6b indicate that precipitation reaches the surface after 14 h. Since the first two range bins of the profile were excluded, the CBH is located at 60 m in such conditions.

In both cases, the PT CBH is significantly lower compared to the Vaisala and THT CBH. At both study sites, the Vaisala CBH is situated much higher in the actual cloud, where backscatter values are highest most of the time. This is to be expected since the primary goal of the Vaisala algorithm is to detect visibility changes for pilots. In the case

AMTD
6, 9819–9855, 2013

of optically thin features with only low backscatter values, Vaisala sometimes reports the profile as being clear sky. The THT algorithm detects hydrometeors more often, but the CBH is often placed higher as well. THT takes into account the first derivative of the backscatter profile, while optically thin ice clouds are not characterized by a sharp increase in backscatter. The PT algorithm is more sensitive and is triggered by optically thinner hydrometeor layers. The number of cloudy profiles reported by PT therefore is higher and the detected CBH is reported at lower altitudes. The sensitive nature of the PT algorithm indicates that the noise reduction and averaging procedures have to be an inherent part of the algorithm itself to avoid false triggering by noise signals.

4.2 Comparison with radiosondes

Atmospheric sounding by radiosondes has been used in the past for cloud detection validation in polar regions, where higher values of RH are associated with clouds (Gettelman et al., 2006; Minnis et al., 2005; Tapakis and Charalambides, 2012). The RH at the level of the detected CBH should in general be high, assuming the actual presence of hydrometeors at this height. An example case with ceilometer attenuated backscatter measurements and the radiosonde-derived RH_{ice} is shown in Fig. 7, which shows that the RH_{ice} increases significantly at the cloud base.

To assess how the PT algorithm performs, we therefore estimated in a statistical analysis the difference in RH_{ice} measurements at the detected cloud base vs. RH_{ice} measurements in clear sky profiles. In order to make this analysis as objective as possible, we first derived a probability distribution for the detected CBH over all cases. Then, we randomly selected RH_{ice} measurements in clear sky profiles following the same probability distribution in order to set up a sample with an equal amount of clear sky RH_{ice} measurements at identical altitudes compared to the CBH RH_{ice} measurements. The result is two samples of RH_{ice} measurements at the cloud base vs. clear sky, selected at the same altitudes with an equal number of observations in each.

AMTD
6, 9819–9855, 2013

The histograms of the two samples (clear sky and cloud base) are plotted in Fig. 8. The green bars indicate occurrences in a RH_{ice} interval for the clear sky sample. Blue bars represent occurrences in a RH_{ice} interval for the cloud base sample. It shows that when a cloud base is detected, RH_{ice} at this cloud base is mostly around 100 % with only very few cases lower than 80 %. For clear sky, on the other hand, the radiosonde also detects high RH_{ice}, although more occurrences at very low RH_{ice} values are present. The high abundance of large RH_{ice} values in clear sky conditions is related to the high fraction of cloud bases near the surface (Sect. 4.4). Shupe et al. (2013) found that in this region RH_{ice} values are typically high due to the frequent occurrence of moisture inversions near the surface. According to Vömel et al. (2007), a possible dry bias in the RH measurements of the RS92 radiosonde is smallest at low altitudes, suggesting that our conclusions should not be influenced significantly by a possible bias.

We used a one-sided nonparametric two-sample Kolmogorov–Smirnov test to determine if the RH_{ice} measurements of cloud bases were significantly higher compared to clear sky RH_{ice} values (Hájek et al., 1967). The test indicates that the cloud base RH_{ice} values are indeed significantly higher than the clear sky RH_{ice} values (p value < 0.01), suggesting that the PT algorithm performs well.

4.3 Optical depth of detected features

Translating the attenuated backscatter values of the detected hydrometeor layers to optical depths allows a physical interpretation of what the PT algorithm actually detects. Such translation however is not straightforward since the optical depth depends strongly on the properties of the cloud (Tselioudis et al., 1992; King et al., 1998; Kay et al., 2006) and the calculation of optical depth requires the corrected backscatter coefficients and this correction of the observed backscatter for attenuation of the signal is based on knowledge of the extinction profile which is unknown. The corrected backscatter was estimated following the procedure described by Platt (1979). This procedure starts with Eq. (2), which describes the relation between observed

AMTD
6, 9819–9855, 2013

attenuated backscatter at a height z ($\beta_{\mathrm{att},z}$) and the true backscatter coefficient at this height corrected for attenuation (β_z):

$$\beta_z = \frac{\beta_{\mathrm{att},z}}{\exp(-2 \times \tau_z)}. \quad (2)$$

In this equation, the exponential term describes the two-way attenuation in the profile between the cloud base (z_0) and height z and τ_z is the optical thickness along the path calculated as:

$$\tau_z = \int_{z_0}^{z} \sigma \mathrm{d}z' = \int_{z_0}^{z} S \times \beta_{z'} \mathrm{d}z', \quad (3)$$

where σ is the extinction coefficient and S is the extinction-to-backscatter ratio (lidar ratio). S depends on numerous factors, including size distribution, composition and shape of the particles (Heymsfield and Platt, 1984; Chen et al., 2002). Yorks et al. (2011) found a constant lidar ratio of $S = 16$ sr for liquid altocumulus clouds and $S = 25$ sr for ice clouds. As our measurements include a variety of atmospheric conditions from ice to supercooled liquid, we assume an average ratio of $S = 20$ sr for a rough estimation of the extinction coefficient. After combining Eqs. (2) and (3), the final equation is described by Eq. (4):

$$\beta_z = \frac{\beta_{\mathrm{att},z}}{\exp\left(-2 \times S \times \int_{z_0}^{z} \beta_{z'} \mathrm{d}z'\right)}. \quad (4)$$

The procedure assumes that at the cloud base $\beta_{z_0} = \beta_{\mathrm{att},z_0}$, since attenuation of the signal under the cloud base is negligible. Next, the cloud is divided into a number of thin layers, corresponding to the range bins of the ceilometer. The integral in Eq. (4) is discretized and the corrected backscatter coefficients of the range bins are

AMTD
6, 9819–9855, 2013

successively calculated until the upper end of the profile is reached. In the procedure, the effects of multiple scattering are not taken into account. In a final step, the optical depth τ of the detected cloud is cumulatively calculated for the successive range bins, using Eq. (3).

The assumptions for both the lidar ratio S and the derivation of the corrected backscatter from observed backscatter make the optical depth calculations prone to a considerate degree of uncertainty. Despite many assumptions simplifying a complex problem, this procedure allows us to make a rough estimation of the optical depth of hydrometeor layers detected by the PT algorithm.

We found at Summit optical depths detected by the PT algorithm as low as $\tau = 0.01$ and 32 % of the detected hydrometeor features attenuated the laser beam ($\tau > 3$, in accordance with Sassen and Cho, 1992). At PE, the lower limit of optical depths was 0.01 as well, while 21 % of the detections attenuated the laser beam. The drawback of the high sensitivity of the algorithm (detection of features with $\tau = 0.01$) is that CBH detection can sometimes be triggered by layers of elevated aerosol contents. This only rarely happens over the Antarctic ice sheet due to its remote location and clean air (e.g., Hov et al., 2007). This is not the case for Greenland, which is much closer to industrialized countries. In the events of elevated aerosol contents, some aerosol layers will inherently be identified falsely as cloud (Shupe et al., 2011).

4.4 Application: cloud properties

Cloud height is an important property in cloud statistics. We therefore analysed the detected CBH for all cases at Summit and PE to infer some basic cloud statistics: cloud occurrence fraction and CBH distribution. While the analysis was performed for year-round ceilometer data at Summit (2010–2012), it was constrained to summer observations at PE (December–March, 2010–2013) due to a lack of winter measurements.

The monthly mean cloud cover fraction for Summit was derived by applying the PT algorithm in two modes, once in the sensitive mode using the previously determined

AMTD
6, 9819–9855, 2013

backscatter threshold of $3 \times 10^{-4}\,km^{-1}\,sr^{-1}$ and once using a much higher threshold of $1000 \times 10^{-4}\,km^{-1}\,sr^{-1}$. While the former includes the detection of optically very thin hydrometeors ($\tau \sim 0.01$), the latter is only triggered by clouds that are at least a factor 50 optically thicker ($\tau \sim 0.5$). A threshold of $1000 \times 10^{-4}\,km^{-1}\,sr^{-1}$ has also been used by Hogan et al. (2003) and O'Connor et al. (2004) to identify supercooled liquid layers and they found a minimum optical depth of $\tau = 0.7$ for these clouds.

As shown in Fig. 9, there is no apparent seasonal cycle at Summit in mean monthly cloud cover when including the optically thin hydrometeors, with a year-round cloud cover of 72 %. This is in contrast with Wang and Key (2005) who found in central Greenland the lowest annual mean cloud cover in the Arctic with a value of about 45 %. Such significant difference is probably due to the high amount of optically very thin ice clouds that are easier to be detected by a ground-based ceilometer using a sensitive algorithm compared to a satellite product from AVHRR used by Wang and Key (2005). Our results show similar trends to Shupe et al. (2013) who found an overall high cloud occurrence fraction at Summit combining multiple ground-based instruments. When the optically thin hydrometeors are deliberately excluded, a seasonal cycle emerges with a summer peak of coverage over 40 %, and almost no detections in winter. This agrees with the seasonal distribution of liquid water at Summit (Shupe et al., 2013).

Figure 10a shows that the CBH for both optically thin (solid green line) and thick (solid blue line) hydrometeor layers is close to the surface at Summit, with almost all detections below 500 m (87 %). Shupe et al. (2011) found a monthly mean CBH below roughly 1 km in all months at Summit. The effect of shallow blowing snow layers in the CBH detection was minimized by excluding the first 60 m of the profile. We found however that 90 % of all profiles with detected hydrometeor layers above 60 m, were in fact affected by a significant backscatter signal in the first 60 m. This suggests that at Summit, hydrometeor layers are most frequently present in the first ranges near the surface and can be associated with various phenomena including fog, snowfall and drifting/blowing snow. The CBH distribution of the remaining 10 % after excluding those profiles affected by hydrometeors in the first 60 m, indicates that some CBH

AMTD
6, 9819–9855, 2013

occurrences are present higher in the profile (∼ 1.5 km, green dashed line in Fig. 10a). Cloud bases of the optically thicker hydrometeors are still below 1 km (blue dashed line).

At PE, we found a mean cloud occurrence fraction in summer of 47 % for hydrometeor layers with optical depths of at least $\tau \sim 0.01$. When including only optically thicker hydrometeor layers ($\tau \geq 0.5$), this fraction reduces to 14 %. The optically thinnest hydrometeors occur mostly near the surface (35 % of all detections below 500 m, solid green line in Fig. 10b) and progressively less frequently higher in the profiles. 80 % of the CBH values of the detected features is below 2 km, of which the 8 March 2010 case in Fig. 6a is a typical example. Using the high backscatter threshold, the resulting CBH detections that are related to optically thicker clouds probably due to supercooled liquid occur mostly (78 %) between 1 km and 3 km (solid blue line). Excluding all profiles that are affected by hydrometeors in the first 60 m reduces the cloud occurrence fraction of all detected clouds to 33 %, meaning that 30 % of all profiles containing a hydrometeor layer are affected by near-surface phenomena such as precipitation and blowing/drifting snow. The CBH distribution of the clouds in profiles not affected by these phenomena shows that the optically thin hydrometeor layers are now slightly higher around 500 m (dashed green line in Fig. 10), while the optically thicker layers are still concentrated in the 1 to 3 km region (dashed blue line).

Overall, most of the CBH results are situated near the surface for both study sites. These findings have important implications with regard to other remote sensing instruments that are used to study these areas. For example, satellite sensors such as CloudSat carrying an active radar with a blind zone in the lowest ranges due to surface reflection (Marchand et al., 2008), have to take into account that an important part of the hydrometeor layers is situated near the surface.

AMTD
6, 9819–9855, 2013

5 Conclusions

The importance of polar clouds for the energy and mass balance of the ice sheets indicates the need for an improved understanding of macro- and microphysical cloud properties. The ceilometer, which is one of the more abundant ground-based instruments in polar regions, can be used to detect cloud bases. The standard algorithms however fail to report the frequently occurring optically thin ice layers, as they are primarily designed to detect strong visibility changes. In this paper, we propose the new Polar Threshold algorithm that uses a backscatter threshold and is developed to be sensitive to optically thin hydrometeors. The optimal attenuated backscatter threshold of $3 \times 10^{-4}\,\mathrm{km}^{-1}\,\mathrm{sr}^{-1}$ was objectively determined by a sensitivity analysis on all available cases for the Princess Elisabeth station in the escarpment zone of East Antarctica and the Summit station in the interior of Greenland. After noise reduction and averaging procedures, the algorithm was shown to identify hydrometeor features with optical depths as low as 0.01. Comparison with observations by radiosondes at Summit indicated that the observed $\mathrm{RH}_{\mathrm{ice}}$ was significantly higher at the cloud base than in clear sky conditions, suggesting that the PT algorithm can successfully differentiate between clear sky and cloudy conditions. Mean cloud cover fraction at Summit is relatively constant year-round when the optically thin hydrometeors are included. Optically thicker features (backscatter threshold $1000 \times 10^{-4}\,\mathrm{km}^{-1}\,\mathrm{sr}^{-1}$), most probably related to supercooled liquid droplets, show however a clear seasonal cycle with a significantly higher cloud cover fraction in summer compared to winter. The greatest part of all cloud detections at Summit was found near the surface. At Princess Elisabeth, the optically thinnest features occur mostly near the surface as well while optically thicker hydrometeor layers occur higher in the profile, mostly between 1 km and 3 km above the surface. The high abundance of hydrometeors in the lowest ranges has important implications, for example when using satellite observations such as CloudSat's active radar which may be insensitive to near-surface hydrometeors due to surface reflection of the signal. This study indicates that using an adapted algorithm

AMTD
6, 9819–9855, 2013

for cloud base height detection, the robust and relatively low-cost ceilometer can be successfully used to extract information on a wide range of hydrometeor types over the ice sheets, including the frequently occurring optically thin ice layers.

Acknowledgements. KVT is a research fellow at the Research Foundation Flanders (FWO). SL was supported in the framework of project GO-OA-25 funded by Netherlands Organisation for Scientific Research (NWO) and as postdoctoral researcher for the FWO. IG was supported via the project HYDRANT funded by the Belgian Science Policy Office under grant number EN/01/4B, in the frame of which PE measurements were performed. The Summit data were recorded in the frame of the ICECAPS project, which is supported by the US National Science Foundation under Grants ARC-0856773, 0904152, and 0856559 as part of the Arctic Observing Network (AON) program, with additional instrumentation provided by the NOAA Earth System Research Laboratory, US Department of Energy ARM Program, and Environment Canada. We are grateful to Christoph Münkel and Reijo Roininen (Vaisala) for continuing support of PE ceilometer and Giovanni Martucci (National University of Ireland) for providing the THT code. We would also like to thank the International Polar Foundation for logistical support at PE and Alexander Mangold (RMI) for help with the HYDRANT instrument maintenance.

References

Barnes, J. E., Bronner, S., Beck, R., and Parikh, N. C.: Boundary Layer Scattering Measurements with a Charge-Coupled Device Camera Lidar, Appl. Optics, 42, 2647, doi:10.1364/AO.42.002647, 2003. 9823

Bennartz, R., Shupe, M. D., Turner, D. D., Walden, V. P., Steffen, K., Cox, C. J., Kulie, M. S., Miller, N. B., and Pettersen, C.: July 2012 Greenland melt extent enhanced by low-level liquid clouds, Nature, 496, 83–86, doi:10.1038/nature12002, 2013. 9821

Bernhard, G.: Version 2 data of the national science foundation's ultraviolet radiation monitoring network: South Pole, J. Geophys. Res., 109, D21207, doi:10.1029/2004JD004937, 2004. 9822

Bintanja, R. and Van den Broeke, M. R.: The influence of clouds on the radiation budget of ice and snow surfaces in Antarctica and Greenland in summer, Int. J. Climatol., 16, 1281–1296, doi:10.1002/(SICI)1097-0088(199611)16:11<1281::AID-JOC83>3.0.CO;2-A, 1996. 9821, 9826

AMTD

6, 9819–9855, 2013

Bromwich, D. H., Nicolas, J. P., Hines, K. M., Kay, J. E., Key, E. L., Lazzara, M. A., Lubin, D., McFarquhar, G. M., Gorodetskaya, I. V., Grosvenor, D. P., Lachlan-Cope, T., and van Lipzig, N. P. M.: Tropospheric clouds in Antarctica, Rev. Geophys., 50, RG1004, doi:10.1029/2011RG000363, 2012. 9821, 9822, 9826

Campbell, J. R., Hlavka, D. L., Welton, E. J., Flynn, C. J., Turner, D. D., Spinhirne, J. D., Scott, V. S., and Hwang, I. H.: Full-time, eye-safe cloud and aerosol lidar observation at atmospheric radiation measurement program sites: instruments and data processing, J. Atmos. Ocean. Tech., 19, 431–442, doi:10.1175/1520-0426(2002)019<0431:FTESCA>2.0.CO;2, 2002. 9822

Chen, W.-N., Chiang, C.-W., and Nee, J.-B.: Lidar ratio and depolarization ratio for cirrus clouds, Appl. Optics, 41, 6470–6476, doi:10.1364/AO.41.006470, 2002. 9833

Clothiaux, E. E., Mace, G. G., Ackerman, T. P., Kane, T. J., Spinhirne, J. D., and Scott, V. S.: An automated algorithm for detection of hydrometeor returns in micropulse lidar data, J. Atmos. Ocean. Tech., 15, 1035–1042, doi:10.1175/1520-0426(1998)015<1035:AAAFDO>2.0.CO;2, 1998. 9822, 9827

Curry, J. A., Schramm, J. L., Rossow, W. B., and Randall, D.: Overview of Arctic cloud and radiation characteristics, J. Climate, 9, 1731–1764, doi:10.1175/1520-0442(1996)009<1731:OOACAR>2.0.CO;2, 1996. 9822, 9826

Curry, J. A., Hobbs, P. V., King, M. D., Randall, D. A., Minnis, P., Isaac, G. A., Pinto, J. O., Uttal, T., Bucholtz, A., Cripe, D. G., Gerber, H., Fairall, C. W., Garrett, T. J., Hudson, J., Intrieri, J. M., Jakob, C., Jensen, T., Lawson, P., Marcotte, D., Nguyen, L., Pilewskie, P., Rangno, A., Rogers, D. C., Strawbridge, K. B., Valero, F. P. J., Williams, a. G., and Wylie, D.: FIRE Arctic Clouds Experiment, B. Am. Meteorol. Soc., 81, 5–29, doi:10.1175/1520-0477(2000)081<0005:FACE>2.3.CO;2, 2000. 9822

Dufresne, J.-L. and Bony, S.: An assessment of the primary sources of spread of global warming estimates from coupled atmosphere–ocean models, J. Climate, 21, 5135–5144, doi:10.1175/2008JCLI2239.1, 2008. 9821

Ettema, J., van den Broeke, M. R., van Meijgaard, E., van de Berg, W. J., Box, J. E., and Steffen, K.: Climate of the Greenland ice sheet using a high-resolution climate model – Part 1: Evaluation, The Cryosphere, 4, 511–527, doi:10.5194/tc-4-511-2010, 2010. 9821

Flynn, C.: Vaisala ceilometer (model CT25K) handbook, ARM TR-020, available at: http://www.wmo.int/pages/prog/gcos/documents/gruanmanuals/Z_instruments/vceil_handbook.pdf (last access: 4 October 2013), 2004. 9822, 9826

AMTD
6, 9819–9855, 2013

Garrett, T. J. and Zhao, C.: Ground-based remote sensing of thin clouds in the Arctic, Atmos. Meas. Tech., 6, 1227–1243, doi:10.5194/amt-6-1227-2013, 2013. 9822
Gettelman, A., Walden, V. P., Miloshevich, L. M., Roth, W. L., and Halter, B.: Relative humidity over Antarctica from radiosondes, satellites, and a general circulation model, J. Geophys. Res., 111, D09S13, doi:10.1029/2005JD006636, 2006. 9831
Gorodetskaya, I. V., Tremblay, L.-B., Liepert, B., Cane, M. A., and Cullather, R. I.: The influence of cloud and surface properties on the Arctic Ocean shortwave radiation budget in coupled models, J. Climate, 21, 866–882, doi:10.1175/2007JCLI1614.1, 2008. 9821
Gorodetskaya, I. V., Van Lipzig, N. P. M., Van den Broeke, M. R., Mangold, A., Boot, W., and Reijmer, C. H.: Meteorological regimes and accumulation patterns at Utsteinen, Dronning Maud Land, East Antarctica: analysis of two contrasting years, J. Geophys. Res.-Atmos., 118, 1700–1715, doi:10.1002/jgrd.50177, 2013a. 9823, 9829
Gorodetskaya I. V., Van Lipzig, N. P. M., Kneifel, S., Maahn, M ., Van Tricht, K., Schween, J. H., and Crewell, S.: Cloud and precipitation properties from ground-based remote sensing in East Antarctica, The Cryosphere, in preparation, 2013b 9823
Hájek, J., Šidák, Z., and Sen, P.: Theory of Rank Tests, Academic press, New York, available at: http://www.library.wisc.edu/selectedtocs/bb596.pdf (last access: 13 September 2013), 1967. 9832
Heese, B., Flentje, H., Althausen, D., Ansmann, A., and Frey, S.: Ceilometer lidar comparison: backscatter coefficient retrieval and signal-to-noise ratio determination, Atmos. Meas. Tech., 3, 1763–1770, doi:10.5194/amt-3-1763-2010, 2010. 9827, 9828
Heymsfield, A. J. and Platt, C. M. R.: A parameterization of the particle size spectrum of ice clouds in terms of the ambient temperature and the ice water content, J. Atmos. Sci., 41, 846–855, doi:10.1175/1520-0469(1984)041<0846:APOTPS>2.0.CO;2, 1984. 9833
Hobbs, P. V. and Rangno, A. L.: Microstructures of low and middle-level clouds over the Beaufort Sea, Q. J. Roy. Meteor. Soc., 124, 2035–2071, doi:10.1002/qj.49712455012, 1998. 9822
Hogan, R. J., Illingworth, a. J., O'Connor, E. J., and PoiaresBaptista, J. P. V.: Characteristics of mixed-phase clouds. II: A climatology from ground-based lidar, Q. J. Roy. Meteor. Soc., 129, 2117–2134, doi:10.1256/qj.01.209, 2003. 9821, 9835
Hov, O. Y., Shepson, P., and Wolff, E.: The chemical composition of the polar atmosphere – the IPY contribution, WMO Bulletin, 56, 263–269, 2007. 9834
Intrieri, J. M.: An annual cycle of Arctic surface cloud forcing at SHEBA, J. Geophys. Res., 107, 8039, doi:10.1029/2000JC000439, 2002. 9821, 9826

AMTD
6, 9819–9855, 2013

Kay, J. E. and L'Ecuyer, T.: Observational constraints on Arctic Ocean clouds and radiative fluxes during the early 21st century, J. Geophys. Res.-Atmos., 118, 7219–7236, doi:10.1002/jgrd.50489, 2013. 9821, 9822

Kay, J. E., Baker, M., and Hegg, D.: Microphysical and dynamical controls on cirrus cloud optical depth distributions, J. Geophys. Res., 111, D24205, doi:10.1029/2005JD006916, 2006. 9832

King, M. D., Tsay, S. C., Platnick, S. E., Wang, M., and Liou, K.-N.: Cloud retrieval algorithms for MODIS: optical thickness, effective particle radius, and thermodynamic phase, in: Algorithm Theor. Basis Doc. ATBD-MOD-05, NASA Goddard Space Flight Cent., Greenbelt, MD, available at: http://www.modis.whu.edu.cn/chinese/context/info/atmosphere/atmosphere_optical_mod05.pdf (last access: 13 September 2013), 1998. 9832

Lubin, D., Chen, B., Bromwich, D. H., Somerville, R. C. J., Lee, W.-H., and Hines, K. M.: The impact of antarctic cloud radiative properties on a GCM climate simulation, J. Climate, 11, 447–462, doi:10.1175/1520-0442(1998)011<0447:TIOACR>2.0.CO;2, 1998. 9821

Marchand, R., Mace, G. G., Ackerman, T., and Stephens, G.: Hydrometeor detection using Cloudsat – an Earth-orbiting 94-GHz cloud radar, J. Atmos. Ocean. Tech., 25, 519–533, doi:10.1175/2007JTECHA1006.1, 2008. 9836

Martucci, G., Milroy, C., and O'Dowd, C. D.: Detection of cloud-base height using Jenoptik CHM15K and Vaisala CL31 ceilometers, J. Atmos. Ocean. Tech., 27, 305–318, doi:10.1175/2009JTECHA1326.1, 2010. 9822, 9826

Miloshevich, L. M., Vömel, H., Paukkunen, A., Heymsfield, A. J., and Oltmans, S. J.: Characterization and correction of relative humidity measurements from Vaisala RS80-A radiosondes at cold temperatures, J. Atmos. Ocean. Tech., 18, 135–156, doi:10.1175/1520-0426(2001)018<0135:CACORH>2.0.CO;2, 2001. 9826

Minnis, P., Yi, Y., Huang, J., and Ayers, K.: Relationships between radiosonde and RUC-2 meteorological conditions and cloud occurrence determined from ARM data, J. Geophys. Res., 110, D23204, doi:10.1029/2005JD006005, 2005. 9831

Münkel, C., Eresmaa, N., Räsänen, J., and Karppinen, A.: Retrieval of mixing height and dust concentration with lidar ceilometer, Bound.-Lay. Meteorol., 124, 117–128, doi:10.1007/s10546-006-9103-3, 2006. 9824, 9827

Murray, F. W.: On the computation of saturation vapor pressure, J. Appl. Meteorol., 6, 203–204, doi:10.1175/1520-0450(1967)006<0203:OTCOSV>2.0.CO;2, 1967. 9826

AMTD
6, 9819–9855, 2013

O'Connor, E. J., Illingworth, A. J., and Hogan, R. J.: A technique for autocalibration of cloud lidar, J. Atmos. Ocean. Tech., 21, 777–786, doi:10.1175/1520-0426(2004)021<0777:ATFAOC>2.0.CO;2, 2004. 9825, 9835

Pattyn, F., Matsuoka, K., and Berte, J.: Glacio-meteorological conditions in the vicinity of the Belgian Princess Elisabeth Station, Antarctica, Antarct. Sci., 22, 79–85, doi:10.1017/S0954102009990344, 2009. 9823

Pinto, J. O.: Autumnal mixed-phase cloudy boundary layers in the Arctic, J. Atmos. Sci., 55, 2016–2038, doi:10.1175/1520-0469(1998)055<2016:AMPCBL>2.0.CO;2, 1998. 9822

Platt, C. M. R.: Remote sounding of high clouds: I. calculation of visible and infrared optical properties from lidar and radiometer measurements, J. Appl. Meteorol., 18, 1130–1143, doi:10.1175/1520-0450(1979)018<1130:RSOHCI>2.0.CO;2, 1979. 9832

Platt, C. M., Young, S. A., Carswell, A. I., Pal, S. R., McCormick, M. P., Winker, D. M., DelGuasta, M., Stefanutti, L., Eberhard, W. L., Hardesty, M., Flamant, P. H., Valentin, R., Forgan, B., Gimmestad, G. G., Jäger, H., Khmelevtsov, S. S., Kolev, I., Kaprieolev, B., Lu, D.-r., Sassen, K., Shamanaev, V. S., Uchino, O., Mizuno, Y., Wandinger, U., Weitkamp, C., Ansmann, A., and Wooldridge, C.: The Experimental Cloud Lidar Pilot Study (ECLIPS) for cloud-radiation research, B. Am. Meteorol. Soc., 75, 1635–1654, doi:10.1175/1520-0477(1994)075<1635:TECLPS>2.0.CO;2, 1994. 9827

Pruppacher, H. and Klett, J.: Microphysics of Clouds and Precipitation, Atmospheric and Oceanographic Sciences Library, Vol. 18, Springer Netherlands, Dordrecht, doi:10.1007/978-0-306-48100-0, 2010. 9822, 9826

Rowe, P. M., Miloshevich, L. M., Turner, D. D., and Walden, V. P.: Dry bias in Vaisala RS90 radiosonde humidity profiles over Antarctica, J. Atmos. Ocean. Tech., 25, 1529–1541, doi:10.1175/2008JTECHA1009.1, 2008. 9826

Roy, G., Vallée, G., and Jean, M.: Lidar-inversion technique based on total integrated backscatter calibrated curves., Appl. Optics, 32, 6754–6763, doi:10.1364/AO.32.006754, 1993. 9829

Sassen, K. and Cho, B. S.: Subvisual-thin cirrus lidar dataset for satellite verification and climatological research, J. Appl. Meteorol., 31, 1275–1285, doi:10.1175/1520-0450(1992)031<1275:STCLDF>2.0.CO;2, 1992. 9834

Sedlar, J., Tjernström, M., Mauritsen, T., Shupe, M. D., Brooks, I. M., Persson, P. O. G., Birch, C. E., Leck, C., Sirevaag, A., and Nicolaus, M.: A transitioning Arctic surface energy

AMTD
6, 9819–9855, 2013

budget: the impacts of solar zenith angle, surface albedo and cloud radiative forcing, Clim. Dynam., 37, 1643–1660, doi:10.1007/s00382-010-0937-5, 2010. 9822
Shanklin, J., Moore, C., and Colwell, S.: Meteorological observing and climate in the British Antarctic Territory and South Georgia: Part 2, Weather, 64, 171–177, doi:10.1002/wea.398, 2009. 9821
Shupe, M. D. and Intrieri, J. M.: Cloud radiative forcing of the Arctic surface: the influence of cloud properties, surface albedo, and solar zenith angle, J. Climate, 17, 616–628, doi:10.1175/1520-0442(2004)017<0616:CRFOTA>2.0.CO;2, 2004. 9822
Shupe, M. D., Walden, V. P., Eloranta, E., Uttal, T., Campbell, J. R., Starkweather, S. M., and Shiobara, M.: Clouds at Arctic atmospheric observatories. Part I: occurrence and macrophysical properties, J. Appl. Meteorol. Clim., 50, 626–644, doi:10.1175/2010JAMC2467.1, 2011. 9821, 9822, 9834, 9835
Shupe, M. D., Turner, D. D., Walden, V. P., Bennartz, R., Cadeddu, M. P., Castellani, B. B., Cox, C. J., Hudak, D. R., Kulie, M. S., Miller, N. B., Neely, R. R., Neff, W. D., and Rowe, P. M.: High and dry: new observations of tropospheric and cloud properties above the Greenland ice sheet, B. Am. Meteorol. Soc., 94, 169–186, doi:10.1175/BAMS-D-11-00249.1, 2013. 9824, 9825, 9832, 9835
Stachlewska, I. S., Piądłowski, M., Migacz, S., Szkop, A., Zielińska, A. J., and Swaczyna, P. L.: Ceilometer observations of the boundary layer over Warsaw, Poland, Acta Geophys., 60, 1386–1412, doi:10.2478/s11600-012-0054-4, 2012 9828
Sun, Z. and Shine, K. P.: Parameterization of ice cloud radiative properties and its application to the potential climatic importance of mixed-phase clouds, J. Climate, 8, 1874–1888, doi:10.1175/1520-0442(1995)008<1874:POICRP>2.0.CO;2, 1995. 9822, 9826
Suortti, T. M., Kivi, R., Kats, A., Yushkov, V., Kämpfer, N., Leiterer, U., Miloshevich, L. M., Neuber, R., Paukkunen, A., Ruppert, P., and Vömel, H.: Tropospheric comparisons of Vaisala radiosondes and balloon-borne frost-point and Lyman-α hygrometers during the LAUTLOS-WAVVAP experiment, J. Atmos. Ocean. Tech., 25, 149–166, doi:10.1175/2007JTECHA887.1, 2008. 9826
Tapakis, R. and Charalambides, A.: Equipment and methodologies for cloud detection and classification: a review, Sol. Energy, 95, 392–430, doi:10.1016/j.solener.2012.11.015, 2012. 9831

AMTD
6, 9819–9855, 2013

Tselioudis, G., Rossow, W. B., and Rind, D.: Global patterns of cloud optical thickness variation with temperature, J. Climate, 5, 1484–1495, doi:10.1175/1520-0442(1992)005<1484:GPOCOT>2.0.CO;2, 1992. 9832

Uttal, T., Curry, J. A., Mcphee, M. G., Perovich, D. K., Moritz, R. E., Maslanik, J. A., Guest, P. S., Stern, H. L., Moore, J. A., Turenne, R., Heiberg, A., Serreze, M. C., Wylie, D. P., Persson, O. G., Paulson, C. A., Halle, C., Morison, J. H., Wheeler, P. A., Makshtas, A., Welch, H., Shupe, M. D., Intrieri, J. M., Stamnes, K., Lindsey, R. W., Pinkel, R., Pegau, W. S., Stanton, T. P., and Grenfeld, T. C.: Surface heat budget of the Arctic Ocean, B. Am. Meteorol. Soc., 83, 255–275, doi:10.1175/1520-0477(2002)083<0255:SHBOTA>2.3.CO;2, 2002. 9822

Verlinde, J., Harrington, J. Y., Yannuzzi, V. T., Avramov, A., Greenberg, S., Richardson, S. J., Bahrmann, C. P., McFarquhar, G. M., Zhang, G., Johnson, N., Poellot, M. R., Mather, J. H., Turner, D. D., Eloranta, E. W., Tobin, D. C., Holz, R., Zak, B. D., Ivey, M. D., Prenni, a. J., DeMott, P. J., Daniel, J. S., Kok, G. L., Sassen, K., Spangenberg, D., Minnis, P., Tooman, T. P., Shupe, M., Heymsfield, a. J., and Schofield, R.: The mixed-phase Arctic cloud experiment, B. Am. Meteorol. Soc., 88, 205–221, doi:10.1175/BAMS-88-2-205, 2007. 9822

Vömel, H., Selkirk, H., Miloshevich, L., Valverde-Canossa, J., Valdés, J., Kyrö, E., Kivi, R., Stolz, W., Peng, G., and Diaz, J. a.: Radiation dry bias of the Vaisala RS92 humidity sensor, J. Atmos. Ocean. Tech., 24, 953–963, doi:10.1175/JTECH2019.1, 2007. 9826, 9832

Wang, J., Zhang, L., Dai, A., Immler, F., Sommer, M., and Vömel, H.: Radiation dry bias correction of Vaisala RS92 humidity data and its impacts on historical radiosonde data, J. Atmos. Ocean. Tech., 30, 197–214, doi:10.1175/JTECH-D-12-00113.1, 2013. 9826

Wang, X. and Key, J. R.: Arctic surface, cloud, and radiation properties based on the AVHRR polar pathfinder dataset. Part I: spatial and temporal characteristics, J. Climate, 18, 2558–2574, doi:10.1175/JCLI3438.1, 2005. 9835

Yorks, J. E., Hlavka, D. L., Hart, W. D., and McGill, M. J.: Statistics of cloud optical properties from airborne lidar measurements, J. Atmos. Ocean. Tech., 28, 869–883, doi:10.1175/2011JTECHA1507.1, 2011. 9833

AMTD
6, 9819–9855, 2013

Table 1. Technical specifications of CT25K (Summit) and CL31 (PE) ceilometers.

Parameter	CT25K	CL31
Wavelength	905 nm	910 nm
Energy per pulse	1.6 ± 20 % µJ	1.2 ± 20 % µJ
Pulse repetition rate	5.57 kHz	10 kHz
Average emitted power	8.9 mW	12 mW
Time resolution	15 s	15 s
Range	7.5 km	7.7 km
Range resolution	30 m	10 m
Backscatter units (precision)	1×10^{-4} km^{-1} sr^{-1}	1×10^{-5} km^{-1} sr^{-1}
Min. detection limit	3×10^{-4} km^{-1} sr^{-1}	1×10^{-5} km^{-1} sr^{-1}
Beam divergence	±0.53 mrad edge, ± 0.75 mrad diagonal	±0.4 mrad edge, ±0.7 mrad diagonal

AMTD
6, 9819–9855, 2013

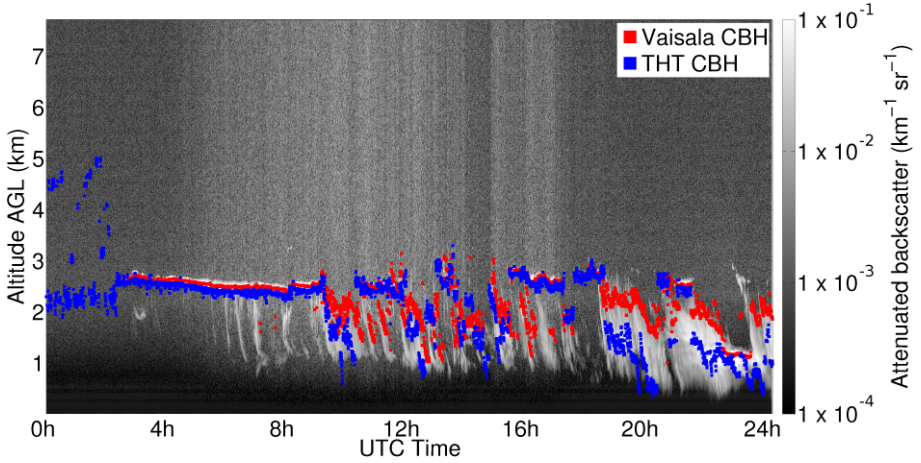

Fig. 1. Ceilometer attenuated backscatter image at Princess Elisabeth (8 March 2010) on a logarithmic scale. Red dots represent the CBH calculated by the built-in Vaisala algorithm. Blue dots represent the CBH calculated by the THT algorithm.

AMTD
6, 9819–9855, 2013

Improved cloud base detection over ice sheets

K. Van Tricht et al.

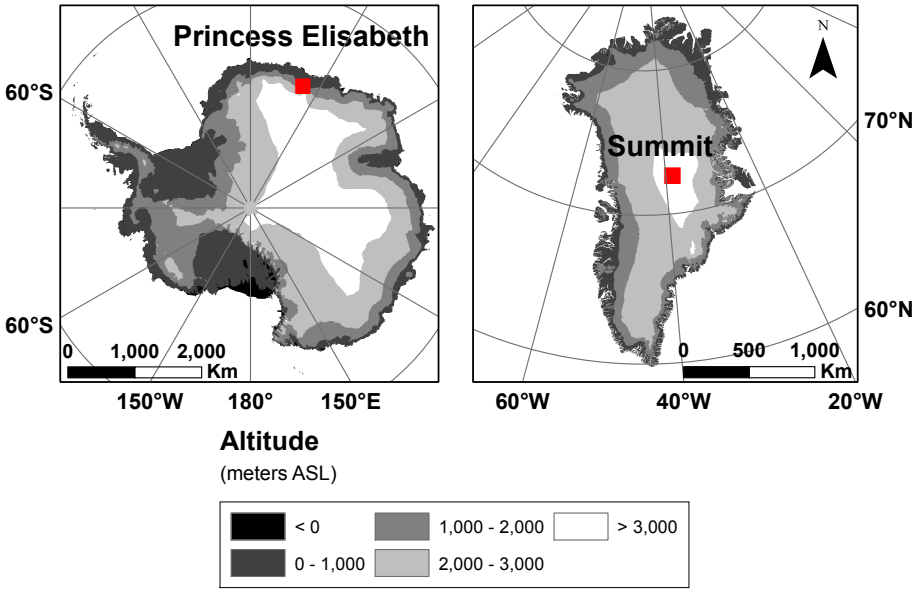

Fig. 2. Locations of PE (Antarctica) and Summit (Greenland) research stations.

AMTD
6, 9819–9855, 2013

Improved cloud base detection over ice sheets

K. Van Tricht et al.

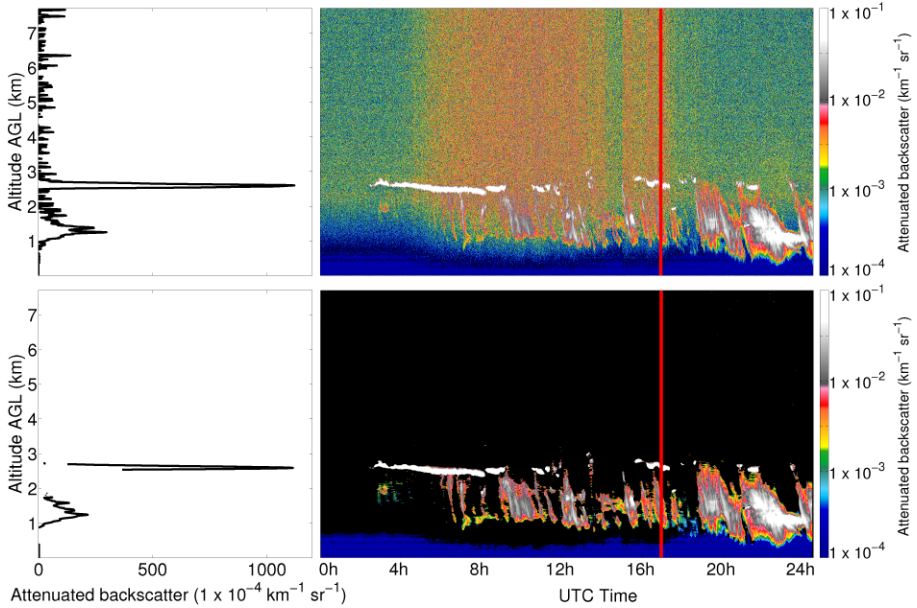

Fig. 3. Ceilometer attenuated backscatter ($km^{-1}\,sr^{-1}$) at PE (8 March 2010) with example profile, indicated by the red line, before (top) and after (bottom) noise reduction and averaging procedures. Range bins where the SNR < 1 are not shown in the lower left image and are plotted in black in the lower right image.

AMTD
6, 9819–9855, 2013

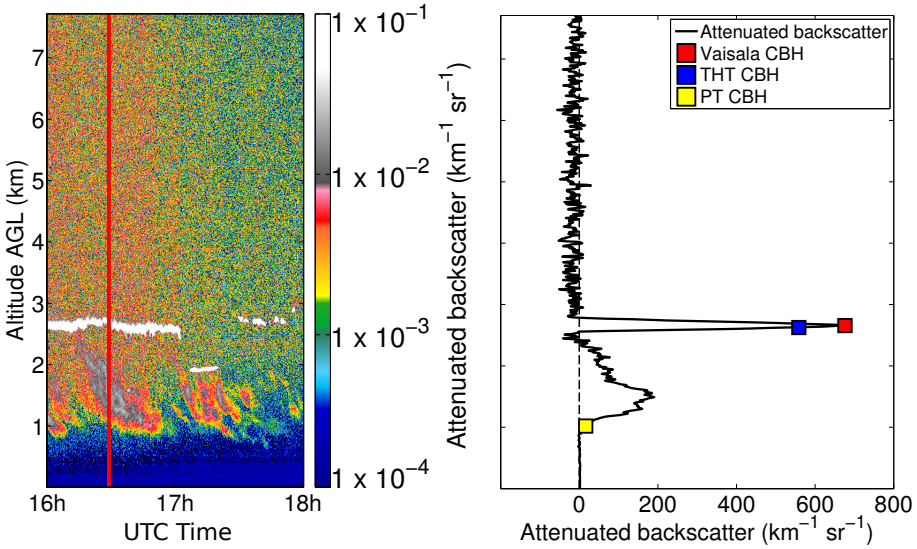

Fig. 4. A time height cross section of attenuated backscatter coefficient (left) and a comparison between Vaisala (red), THT (blue) and PT (yellow) derived CBH in an example attenuated backscatter profile (indicated by red line in the left image) at PE on 8 March 2010 (right). Vaisala and THT report the CBH at high backscatter values. The PT algorithm is triggered at low backscatter values.

AMTD
6, 9819–9855, 2013

Improved cloud base detection over ice sheets

K. Van Tricht et al.

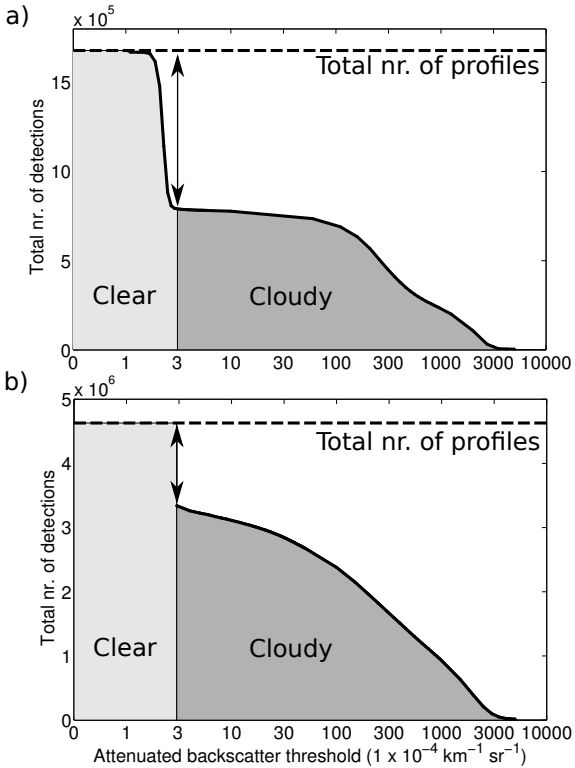

Fig. 5. Sensitivity analyses of backscatter threshold on the cloud detections for **(a)** PE and **(b)** Summit. The dashed line indicates the total amount of profiles that have been tested. The arrows show the amount of profiles marked as clear sky using the chosen threshold. The light grey area represents pixels reported as clear by the PT algorithm, while the dark grey area represents pixels reported as cloudy.

AMTD
6, 9819–9855, 2013

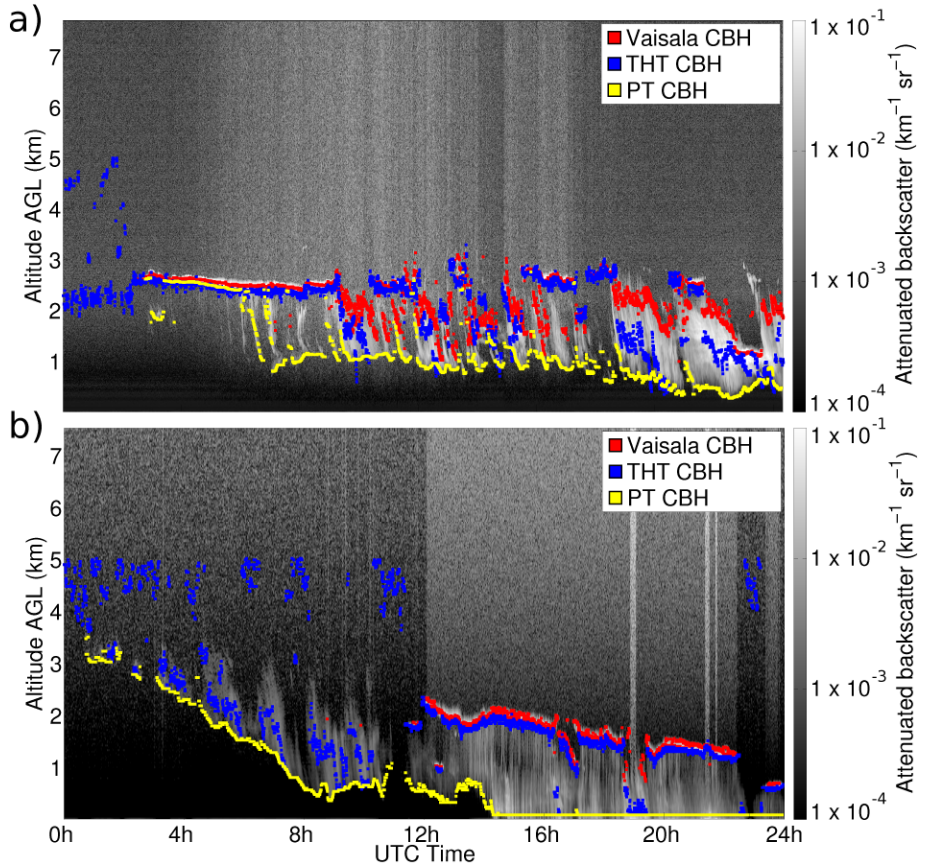

Fig. 6. Comparison of CBH detection results from Vaisala (red), THT (blue) and PT (yellow) algorithms for **(a)** PE ceilometer case of 8 March 2010 and **(b)** Summit ceilometer case of 19 December 2010.

AMTD
6, 9819–9855, 2013

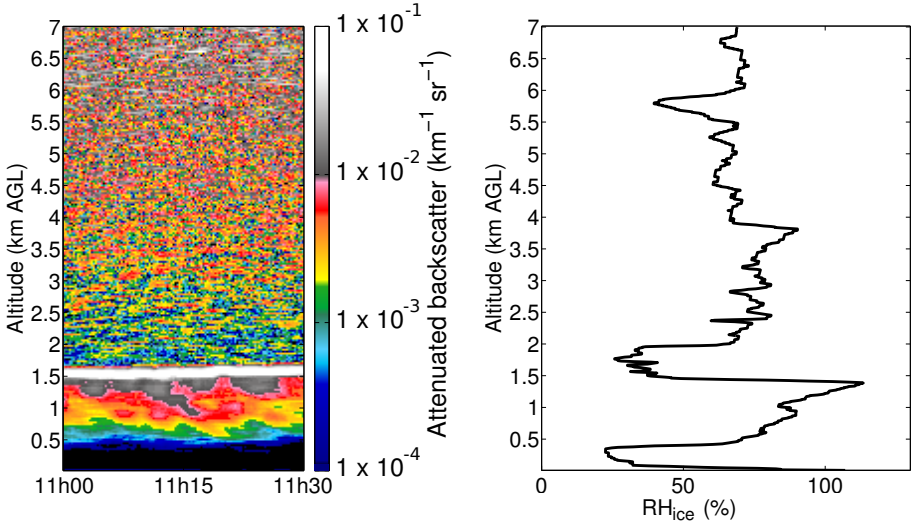

Fig. 7. Comparison between measured attenuated backscatter by ceilometer (left) and RH_{ice} by radiosonde (right) at Summit on 5 August 2011.

AMTD
6, 9819–9855, 2013

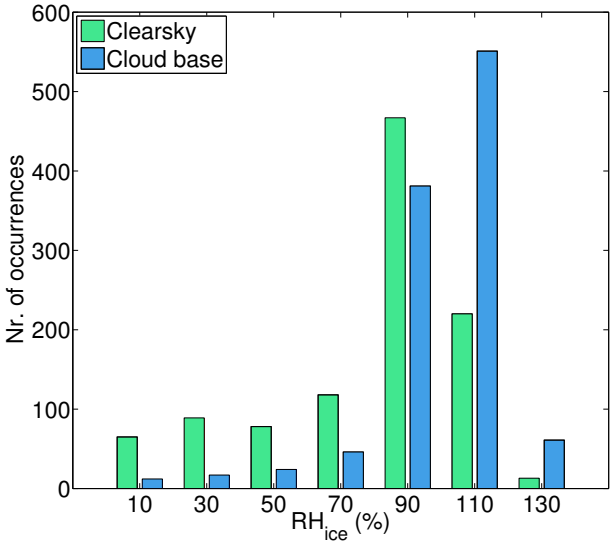

Fig. 8. RH$_{ice}$ measurements of radiosondes for clear sky sample (green bars) and cloud base sample (blue bars). For clear sky the same height distribution was followed as for cloud base. See text for more information.

AMTD
6, 9819–9855, 2013

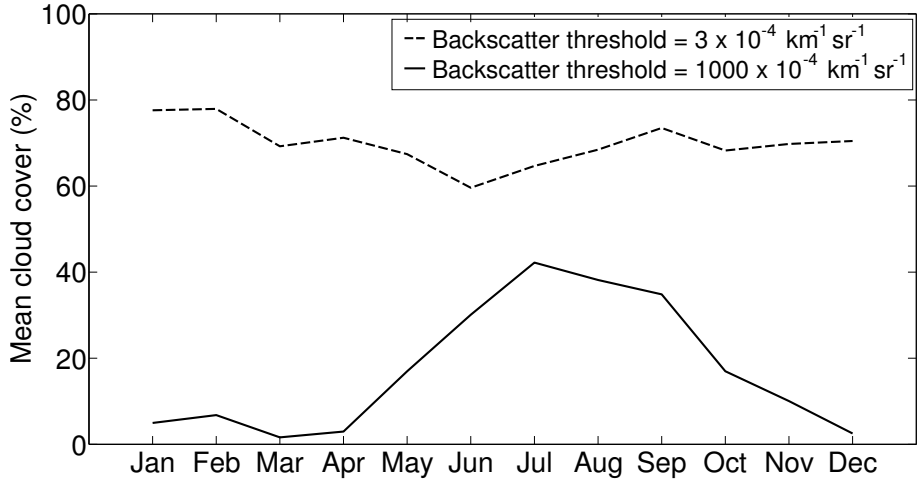

Fig. 9. Monthly mean cloud cover (%) at Summit (2010–2012) derived with sensitive threshold ($3 \times 10^{-4}\,km^{-1}\,sr^{-1}$, dashed line) thereby including optically thin hydrometeor layers and higher threshold ($1000 \times 10^{-4}\,km^{-1}\,sr^{-1}$, solid line) thereby focusing on optically thick hydrometeor layers.

AMTD
6, 9819–9855, 2013

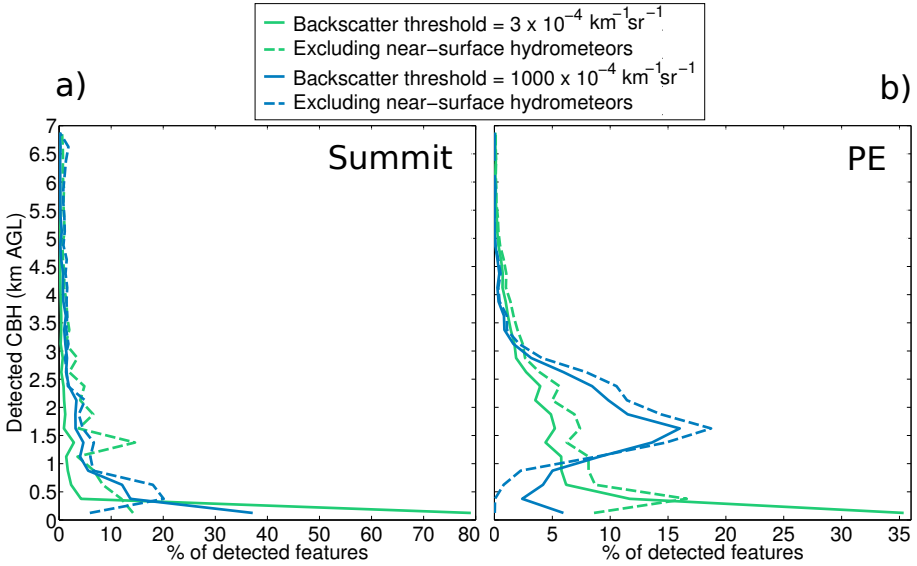

Fig. 10. PT CBH occurrence (%) for low (3×10^{-4} km^{-1} sr^{-1}, green lines) and high (1000×10^{-4} km^{-1} sr^{-1}, blue lines) threshold. Dashed lines indicate CBH occurrence after removing profiles affected by hydrometeors in the first 60 m. **(a)** Analysis for Summit (2010–2012). **(b)** Analysis for PE, with data limited to summer months (2010–2013).

AMTD
6, 9819–9855, 2013